

# Promoting the Intermediates Hydrogenation for Urea Electrosynthesis Over an “Active Hydrogen Pump” Catalyst

Chu Zhang<sup>+</sup>, Quan Zhou<sup>+</sup>, Zeyu Li, Chunshuang Yan,<sup>\*</sup> Hengjie Liu, Daobin Liu,<sup>\*</sup> Li Song, Qingyu Yan,<sup>\*</sup> and Chade Lv<sup>\*</sup>

**Abstract:** Electrocatalytic coupling of CO<sub>2</sub> and NO<sub>3</sub><sup>−</sup> offers a sustainable approach for urea production. However, the limited supply of active hydrogen (\*H) hinders the formation of the key carbon- and nitrogen-containing intermediates, thus impeding the selective C–N coupling. Herein, we developed copper molybdate (Cu<sub>3</sub>Mo<sub>2</sub>O<sub>9</sub>) nanorods, which could serve as “active hydrogen pump” catalysts by regulating the water dissociation and hydrogen adsorption. Such electrocatalyst would guarantee a steady \*H supply for intermediates hydrogenation, hence boosting the generation of \*CO and \*NH<sub>2</sub> intermediates for selective C–N coupling and urea production. In a CO<sub>2</sub>-saturated 0.1 M KNO<sub>3</sub> solution, Cu<sub>3</sub>Mo<sub>2</sub>O<sub>9</sub> achieved a maximum urea yield rate of 177 mmol h<sup>−1</sup> g<sup>−1</sup> with a urea-producing FE of 40% in a flow cell configuration, outperforming most reported electrocatalysts. This study underscores the crucial role of \*H, which may guide the exploration of advanced catalysts for expediting the sustainable synthesis of indispensable chemicals requiring rapid intermediates hydrogenation.

## Introduction

Urea (CO(NH<sub>2</sub>)<sub>2</sub>), a nitrogen fertilizer containing 46% nitrogen, is essential for promoting rapid crop growth and serves as a key feedstock for producing fine chemicals.<sup>[1–4]</sup> However, conventional industrial methods for urea production, such as the Haber–Bosch and Bosch–Meiser processes, are plagued by high energy consumption and massive carbon dioxide emissions.<sup>[5–9]</sup> Developing a clean and efficient technology for urea production under milder conditions is imperative.<sup>[10–12]</sup> Electrosynthesis of urea by coupling CO<sub>2</sub> with NO<sub>3</sub><sup>−</sup> has

recently emerged as a promising alternative under ambient conditions, which environmentally transforms the greenhouse gas and waste streams into value-added product.<sup>[13–16]</sup> Such route involves 16-electron transfer and two C–N coupling steps, accompanied with multiple intermediates that directly lead to complex transform mechanisms.<sup>[17–18]</sup> Substantial challenges remain in realizing selective C–N coupling.<sup>[19–21]</sup>

Given that the key C–N bond formation step is not a proton-coupled electron transfer process, an elegant electrocatalyst should facilitate the generation of intermediates that favor C–N coupling with low energy barrier. Derived from CO<sub>2</sub> and NO<sub>3</sub><sup>−</sup>, \*CO and \*NH<sub>2</sub> that feature the lowest unoccupied molecular orbital (LUMO) in low energy and lone pair of \*NH<sub>2</sub> in high energy, respectively, represent critical intermediates for selective C–N coupling to form \*CONH<sub>2</sub> as suggested by numerous studies. However, the sluggish hydrogenation issue in the electrocatalytic co-reduction of CO<sub>2</sub> and NO<sub>3</sub><sup>−</sup> processes is still remaining, which limits the \*CO and \*NH<sub>2</sub> formation kinetically and also leads to the production of undesired by-products.

Attributed to the moderate binding affinity for both C- and N-intermediates, copper (Cu)-based materials are emerging as active catalysts for electrochemical urea synthesis.<sup>[22–28]</sup> Hu’s group recently created a Cu<sub>AC</sub>–Cu<sub>SA</sub>@NC catalyst,<sup>[29]</sup> which could convert \*NO<sub>3</sub><sup>−</sup> to \*NH<sub>2</sub> through the synergistic effect of the “Cu<sub>AC</sub>” and “Cu<sub>SA</sub>” sites, revealing a relay catalysis process for the co-reduction of CO<sub>2</sub> and NO<sub>3</sub><sup>−</sup>. Zhao et al. constructed an innovative tandem catalyst (RP-AuCu),<sup>[30]</sup> featuring two compatible single-atom active sites of Au and Cu on red phosphorus. The Au sites regulated the CO<sub>2</sub> activation intermediates to generate electrophilic \*COOH, while the Cu active sites enhanced the electrophilic attack of \*COOH species on \*NH<sub>2</sub>, thereby promoting the selective formation of C–N bonds. Nevertheless, pristine

[\*] C. Zhang<sup>+</sup>, Z. Li, Prof. C. Yan, Prof. C. Lv  
 State Key Laboratory of Space Power-Sources, MIIT Key Laboratory of Critical Materials Technology for New Energy Conversion and Storage, School of Chemistry and Chemical Engineering, Harbin Institute of Technology, Harbin 150001, China  
 E-mail: csysan@hit.edu.cn  
 lv.chade@hit.edu.cn

Q. Zhou<sup>+</sup>, Prof. H. Liu, Prof. L. Song  
 National Synchrotron Radiation Laboratory, CAS Center for Excellence in Nanoscience, University of Science and Technology of China, Hefei 230029, China

Prof. D. Liu  
 State Key Laboratory of Precision and Intelligent Chemistry, Hefei National Research Center for Physical Sciences at the Microscale, University of Science and Technology of China, Hefei 230029, China  
 E-mail: ldbin@ustc.edu.cn

Prof. Q. Yan  
 School of Materials Science and Engineering, Nanyang Technological University, Singapore 639798, Singapore  
 E-mail: alexyan@ntu.edu.sg

[+] Both authors contributed equally to this work.

Additional supporting information can be found online in the Supporting Information section

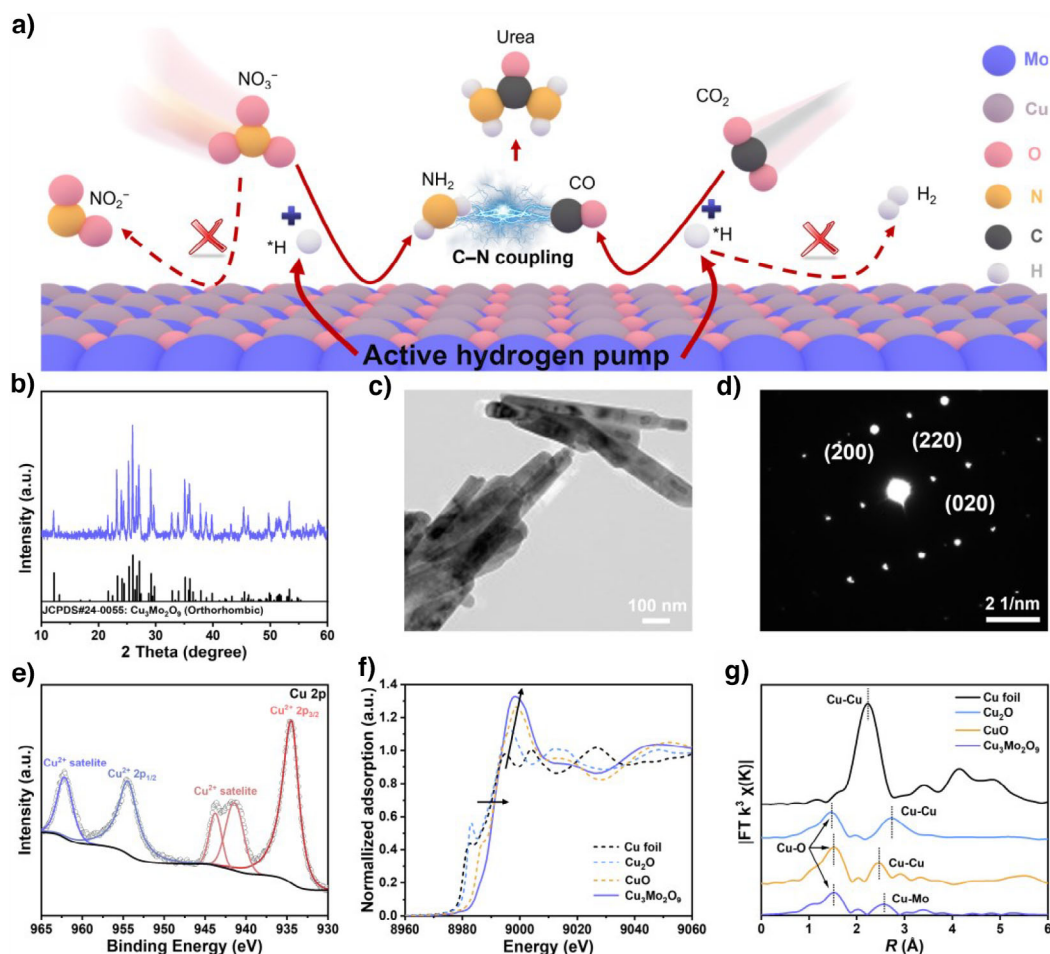


**Figure 1.** Structural and morphological characterization of  $\text{Cu}_3\text{Mo}_2\text{O}_9$ . a) Schematic illustration of urea electro-synthesis facilitated by an "active hydrogen pump" catalyst. b) XRD pattern. c) TEM image and d) corresponding SAED pattern. e) Cu 2p XPS spectrum. f) Cu K-edge XANES spectra. g) R-space EXAFS spectra.

Cu-based catalysts fail in supplying sufficient active hydrogen ( $^*\text{H}$ ) due to its weak hydrogen adsorption ( $\Delta G_{^*\text{H}} > 0$ ),<sup>[31–33]</sup> leading to the preferable production of  $\text{NO}_2^-$  by-product over  $^*\text{NH}_2$  intermediate and low urea yield.<sup>[34]</sup> With the purpose of facilitating the hydrogenation of both  $\text{NO}_3^-$  and  $\text{CO}_2$  on Cu-based catalysts to generate the abovementioned key intermediates, achievable strategy should be proposed to supply sufficient  $^*\text{H}$  for urea electro-synthesis through C–N coupling.

In this work, we proposed a proof-of-concept demonstration by developing a copper molybdate ( $\text{Cu}_3\text{Mo}_2\text{O}_9$ ) nanorod electrocatalyst for urea synthesis through the co-electrolysis of  $\text{NO}_3^-$  and  $\text{CO}_2$  under ambient conditions. Owing molybdenum (Mo), a conventional transitional metal for hydrogen evolution, the  $\text{Cu}_3\text{Mo}_2\text{O}_9$  electrocatalyst could serve as "active hydrogen pump" to guarantee the  $^*\text{H}$  supply (Figure 1a). The hydrogenation of  $\text{NO}_3^-$  and  $\text{CO}_2$  was accordingly boosted over the as-designed  $\text{Cu}_3\text{Mo}_2\text{O}_9$  catalyst, which was elucidated by density functional theory (DFT) calculations in combination with in situ electron paramagnetic resonance (EPR) experiments. A series of in situ analysis, including operando synchrotron-radiation Fourier transform infrared spectroscopy (SR-FTIR), isotope-labelled differen-

tial electrochemical mass spectrometry (DEMS), and in situ Raman analysis, strongly affirmed that  $^*\text{CO}$  and  $^*\text{NH}_2$  were indeed the determinant intermediates for selective C–N coupling. In a  $\text{CO}_2$ -saturated 0.1 M  $\text{KNO}_3$  solution,  $\text{Cu}_3\text{Mo}_2\text{O}_9$  achieved an average urea yield of  $177 \text{ mmol h}^{-1} \text{ g}_{\text{cat}}^{-1}$  with a high Faraday efficiency (FE) of 40% at  $-0.8 \text{ V}$  versus reversible hydrogen electrode (RHE) in a flow cell, outperforming most reported electrocatalysts. This work offers a feasible strategy to overcome limitations in urea electro-synthesis in terms of both yield and selectivity, which may pave the way for developing electrocatalyst toward the synthesis of more value-added chemicals relying on active hydrogen.

## Results and Discussion

### Structural Characterization

The  $\text{Cu}_3\text{Mo}_2\text{O}_9$  catalyst was synthesized from molybdate and cupric acetate via a facile solvothermal process (for details, please Experimental section in the Supporting Information) Analysis using X-ray diffraction (XRD), Raman

spectroscopy, Fourier transform infrared (FTIR) spectroscopy, and inductively coupled plasma atomic emission spectroscopy (ICP-OES) confirmed that the synthesized material was assigned to the  $\text{Cu}_3\text{Mo}_2\text{O}_9$  phase with an orthorhombic structure (Figure 1b and Figure S1, Table S1).<sup>[35,36]</sup> Scanning electron microscopy (SEM) (Figure S2) and transmission electron microscopy (TEM) images revealed that  $\text{Cu}_3\text{Mo}_2\text{O}_9$  exhibited a uniform nanorod morphology (Figure 1c and Figure S3a). High-resolution TEM (HRTEM) image showed interplanar spacings of 3.83 and 7.31 Å, corresponding to the (200) and (020) planes of  $\text{Cu}_3\text{Mo}_2\text{O}_9$ , respectively (Figure S3b). Selected-area electron diffraction (SAED) patterns were utilized to further examine the exposed facets of  $\text{Cu}_3\text{Mo}_2\text{O}_9$ . The rectangular and symmetrical SAED pattern displayed clear diffraction spots corresponding to the (200), (220) and (020) facets of  $\text{Cu}_3\text{Mo}_2\text{O}_9$  (Figure 1d), which could be attributed to the (002) zone-axis diffraction of the orthorhombic phase.

X-ray photoelectron spectroscopy (XPS) and X-ray absorption near-edge structure (XANES) were employed to investigate the chemical state of  $\text{Cu}_3\text{Mo}_2\text{O}_9$ . The Cu 2p spectrum (Figure 1e) displayed two distinct split spin–orbit peaks at 934.5 eV ( $\text{Cu}^{2+} 2p_{3/2}$ ) and 954.6 eV ( $\text{Cu}^{2+} 2p_{1/2}$ ).<sup>[37]</sup> In addition, the peak of Cu Auger LMM spectrum was located at 917.5 eV (Figure S4a). These results indicated the +2 oxidation state of Cu in the  $\text{Cu}_3\text{Mo}_2\text{O}_9$  catalyst.<sup>[38–42]</sup> The XANES analysis further confirmed the Cu valence state as +2, as it almost closely matched the absorption edge of the standard CuO reference (Figure 1f).<sup>[43]</sup> Additionally, Fourier transform extended X-ray absorption fine structure (FT-EXAFS) spectra in R space revealed the prominent peaks at 1.5 and 2.6 Å assignable to Cu–O and Cu–Mo peak in the catalyst, respectively (Figure 1g).<sup>[44]</sup> The Mo 3d XPS spectrum revealed Mo in  $\text{Cu}_3\text{Mo}_2\text{O}_9$  was in the +6 oxidation state with distinct split spin–orbit peaks at 235.5 ( $\text{Mo}^{6+} 3d_{3/2}$ ) and 232.4 eV ( $\text{Mo}^{6+} 3d_{5/2}$ ) (Figure S4b).<sup>[45]</sup> Energy-dispersive X-ray spectroscopy (EDX) elemental mappings showed a uniform distribution of Cu, Mo, and O in  $\text{Cu}_3\text{Mo}_2\text{O}_9$  (Figure S5). To highlight the critical role of as-engineered “active hydrogen pump”  $\text{Cu}_3\text{Mo}_2\text{O}_9$  electrocatalyst, CuO, and  $\text{MoO}_3$  counterparts were also obtained, of which the synthesis details and structural information were presented in supplementary information (Figures S6 and S7).

### Active Hydrogen Mediation Behavior

First, density functional theory (DFT) calculations were performed to determine the availability of active hydrogen. As shown in Figure 2a and Figures S8, the water dissociation ( $\text{*H-OH} \rightarrow \text{*H}$ ) is the rate-determining step (RDS) for CuO with a Gibbs free energy increase ( $\Delta G$ ) of 2.23 eV, implying its weak  $\text{*H}$  generation ability. Although the energy increase for the  $\text{*H}$  generation is much lower on  $\text{MoO}_3$  (0.78 eV), the  $\text{*H} \rightarrow 1/2\text{H}_2$  step only requires a low  $\Delta G$  of 0.84 eV. This suggests the preferable hydrogen evolution reaction on  $\text{MoO}_3$ ,<sup>[46]</sup> which may consume the surface  $\text{*H}$  and provide insufficient active hydrogen.<sup>[47,48]</sup> In sharp contrast, the formation of  $\text{*H}$  is much easier on  $\text{Cu}_3\text{Mo}_2\text{O}_9$  as reflected

in the  $\Delta G$  of  $-1.73$  eV for water dissociation, indicating that  $\text{Cu}_3\text{Mo}_2\text{O}_9$  is equipped with an “active hydrogen pump” for sufficient  $\text{*H}$  supply. In addition, the energy increase of  $\text{*H}$  desorption on  $\text{Cu}_3\text{Mo}_2\text{O}_9$  (1.73 eV) is much higher in contrast with that for  $\text{MoO}_3$  (+0.84 eV). Elucidated by the above theoretical prediction, the  $\text{*H}$  supplied by the “active hydrogen pump”  $\text{Cu}_3\text{Mo}_2\text{O}_9$  electrocatalyst is not favorable for HER, which might be utilized in the hydrogenation processes. To further explore the  $\text{*H}$  generation ability of  $\text{Cu}_3\text{Mo}_2\text{O}_9$ , kinetic isotopic effect (KIE) tests were conducted by replacing  $\text{H}_2\text{O}$  with  $\text{D}_2\text{O}$  to reveal the proton transfer kinetics during the  $\text{H}_2\text{O}$  splitting process.<sup>[48]</sup> The KIE values are determined by comparing the current densities observed in  $\text{H}_2\text{O}$  and  $\text{D}_2\text{O}$  (Figure S9). As displayed in Figure 2b,  $\text{Cu}_3\text{Mo}_2\text{O}_9$  catalyst shows an average KIE value of 1.3, which is much lower than those of CuO (2.1) and  $\text{MoO}_3$  (1.6). This verifies that the hydrolysis process is boosted on  $\text{Cu}_3\text{Mo}_2\text{O}_9$  to facilitate  $\text{*H}$  delivery.

The quasi-in situ electron paramagnetic resonance (EPR) experiments were carried out to investigate the  $\text{*H}$  generation and the subsequent  $\text{*H}$ -mediated process, during which dimethyl-1-pyrrolidine-N-oxide (DMPO) served as the hydrogen radical trapping agent.<sup>[49]</sup> As evidenced by the intense nine-line EPR signals assignable to DMPO-H with a ratio of 1:1:2:1:2:1:2:1:1 in 0.1 M  $\text{Na}_2\text{SO}_4$  electrolyte (Figure 2d),  $\text{Cu}_3\text{Mo}_2\text{O}_9$  enables the production of massive  $\text{*H}$ . Notably, the DMPO-H signals of  $\text{Cu}_3\text{Mo}_2\text{O}_9$  are markedly attenuated upon the addition of  $\text{NO}_3^-$  (0.1 M  $\text{Na}_2\text{SO}_4$  + 0.1 M  $\text{KNO}_3$ ) or  $\text{CO}_2$  (0.1 M  $\text{Na}_2\text{SO}_4$  +  $\text{CO}_2$ ), and completely vanished in the electrolyte containing  $\text{NO}_3^-$  and  $\text{CO}_2$  simultaneously (0.1 M  $\text{KNO}_3$  +  $\text{CO}_2$ ). This suggests the accumulated  $\text{*H}$  will be rapidly consumed by the hydrogenation steps during the co-reduction of  $\text{CO}_2$  and  $\text{NO}_3^-$  process, which might conduce to the generation of key C- and N-containing intermediates for C–N coupling.<sup>[50]</sup> In sharp contrast, CuO fails in the producing  $\text{*H}$  as reflected in the barely detectable DMPO-H signals, in accordance with the theoretical prediction. Unlike  $\text{Cu}_3\text{Mo}_2\text{O}_9$  and CuO,  $\text{MoO}_3$  displays consistently weak signals regardless of the change in electrolyte. This demonstrates that the generated  $\text{*H}$  is more prone to the HER to hamper the hydrogenation of  $\text{NO}_3^-$  and  $\text{CO}_2$ .<sup>[51]</sup> The abovementioned  $\text{*H}$  production and corresponding hydrogenation processes can be further validated by the cyclic voltammetry (CV) tests, in which the characteristic active hydrogen peak is strongly correlated with the surface  $\text{*H}$  content.<sup>[52]</sup> As displayed in Figure 2e,  $\text{Cu}_3\text{Mo}_2\text{O}_9$  displays a significant  $\text{*H}$  signal, of which the intensity decreases drastically in the presence of  $\text{NO}_3^-$  or/and  $\text{CO}_2$ . Under the above conditions, no  $\text{*H}$  signal can be observed for CuO (Figure S10a), which is in agreement with the EPR results. Albeit  $\text{*H}$  emerges for  $\text{MoO}_3$  in 0.1 M  $\text{Na}_2\text{SO}_4$ , the introduction of  $\text{NO}_3^-$  and  $\text{CO}_2$  will not change the  $\text{*H}$  intensity (Figure S10b). This manifests that the  $\text{*H}$  generated on  $\text{MoO}_3$  favors the  $\text{H}_2$  evolution rather than hydrogenation of  $\text{NO}_3^-$  and  $\text{CO}_2$ . Additionally, based on the current densities observed by linear sweep voltammetry (LSV), the  $\text{Cu}_3\text{Mo}_2\text{O}_9$  catalyst exhibits a much lower Tafel slope (218.4  $\text{mV dec}^{-1}$ ) compared to CuO (391.7  $\text{mV dec}^{-1}$ ) and  $\text{MoO}_3$  (780.3  $\text{mV dec}^{-1}$ ) in 0.1 M  $\text{KNO}_3$  with  $\text{CO}_2$



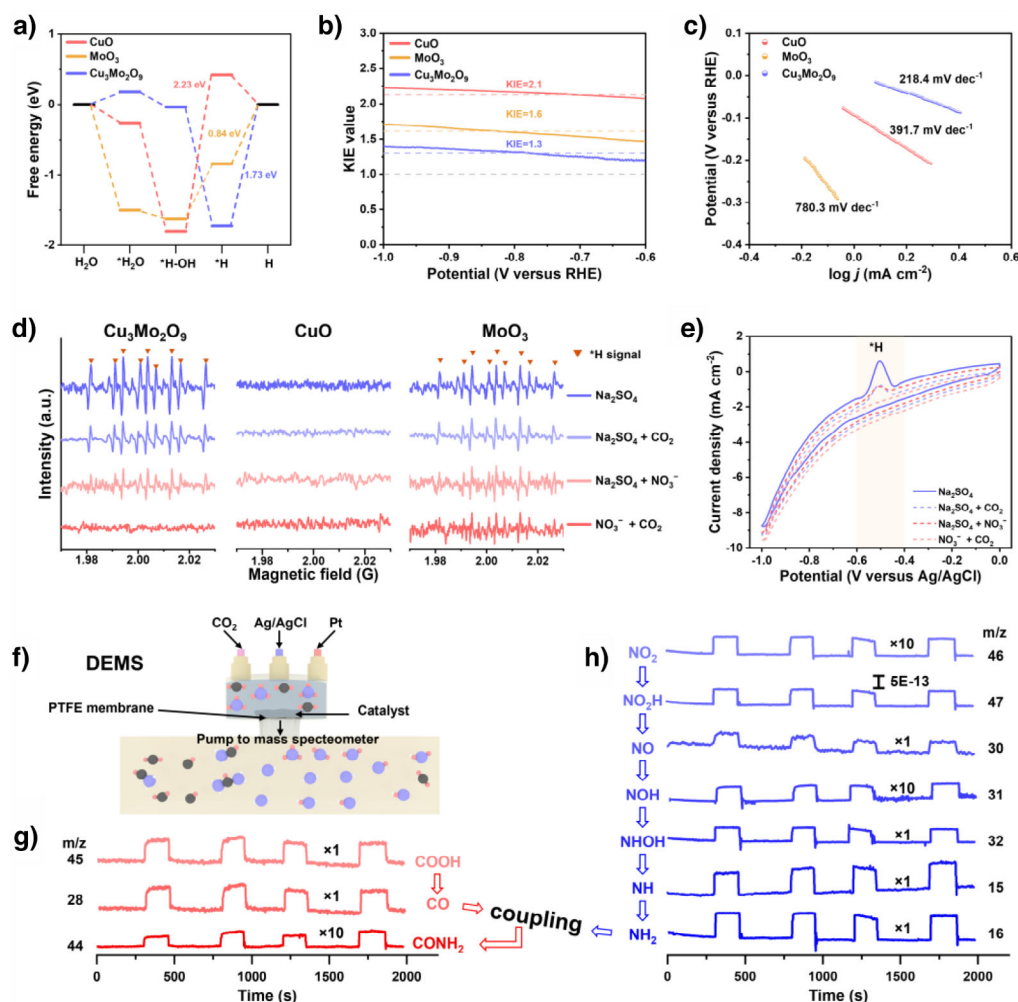


**Figure 2.** Analysis of active hydrogen generation and mediation behaviors. a) Calculated free energy diagrams of HER on  $\text{Cu}_3\text{Mo}_2\text{O}_9$ ,  $\text{CuO}$ , and  $\text{MoO}_3$ . b) KIE tests and c) Tafel plots of  $\text{Cu}_3\text{Mo}_2\text{O}_9$ ,  $\text{CuO}$  and  $\text{MoO}_3$  electrocatalysts. d) Quasi in situ EPR spectra of the solutions obtained after 10 min of electrolytic by  $\text{Cu}_3\text{Mo}_2\text{O}_9$ ,  $\text{CuO}$ , and  $\text{MoO}_3$  at  $-0.8$  V versus RHE using DMPO as the  $\cdot\text{H}$ -trapping reagent. e) Cyclic voltammograms of  $\text{Cu}_3\text{Mo}_2\text{O}_9$  electrocatalyst. f) Schematic diagram of online DEMS technique. Online DEMS signals of g) C- and h) N- intermediates in  $0.1$  M  $\text{KNO}_3$  with  $\text{CO}_2$  bubbling at  $-0.8$  V versus RHE for  $\text{Cu}_3\text{Mo}_2\text{O}_9$ .

bubbling (Figure 2c). This suggests that  $\text{Cu}_3\text{Mo}_2\text{O}_9$  favors both the  $\text{NO}_3\text{RR}$  and  $\text{CO}_2\text{RR}$  processes.<sup>[53]</sup> Indicated by the above comprehensive theoretical analysis and experiment results, the integration of Cu with Mo to synthesize  $\text{Cu}_3\text{Mo}_2\text{O}_9$  can endow the electrocatalyst with “active hydrogen pump”, which not only enables the generation of sufficient  $\cdot\text{H}$ , but also can promote the  $\cdot\text{H}$ -mediated hydrogenation of  $\text{CO}_2$  and  $\text{NO}_3^-$ . Attributed to the sufficient  $\cdot\text{H}$  supply for the hydrogenation of both the  $\text{NO}_3^-$  and  $\text{CO}_2$ , as-developed electrocatalyst may accelerate the generation of key C- and N-containing intermediates for selective urea electrosynthesis.<sup>[54]</sup>

### Mechanism Investigations in C–N Coupling

To monitor the C- and N-containing intermediates and determine the possible C–N coupling pathway on the  $\text{Cu}_3\text{Mo}_2\text{O}_9$  catalyst, online DEMS was implemented (for details, please

refer to the experimental section in Supplementary Information) (Figure 2f). As proved by the signals of  $\text{COOH}^+$  ( $m/z = 45$ ) and  $\text{CO}^+$  ( $m/z = 28$ ), the electrocatalytic  $\text{CO}_2\text{RR}$  process follows the “ $\text{CO}_2 \rightarrow \cdot\text{COOH} \rightarrow \cdot\text{CO}$ ” pathway (Figure 2g). Meanwhile, various N-containing intermediates signals are also observed (Figure 2h), which confirms the pathway of “ $\text{NO}_3^- \rightarrow \cdot\text{NO}_2\text{H} \rightarrow \cdot\text{NO} \rightarrow \cdot\text{NOH} \rightarrow \cdot\text{NHOH} \rightarrow \cdot\text{NH} \rightarrow \cdot\text{NH}_2$ ” toward electrocatalytic  $\text{NO}_3\text{RR}$  process. Apart from the above intermediates derived from individual  $\text{CO}_2\text{RR}$  and  $\text{NO}_3\text{RR}$  processes, the  $m/z = 44$  signal assignable to the  $\text{CONH}_2^+$  can also be detected. It demonstrates that the formation of C–N bond is realized by coupling  $\cdot\text{CO}$  with  $\cdot\text{NH}_2$  intermediates. No detectable  $\text{CONH}^+$  ( $m/z = 43$ ) signal excludes the possible C–N coupling pathway with  $\cdot\text{CO}$  and  $\cdot\text{NH}$  intermediates (Figure S11). As reflected in the DEMS results for  $\text{CuO}$  and  $\text{MoO}_3$ , nevertheless, the  $\text{CONH}_2^+$  signal is not detected, which might be attributed to the insufficient supply of key C- and N-containing intermediates for C–N coupling (Figures S12 and S13). When performing

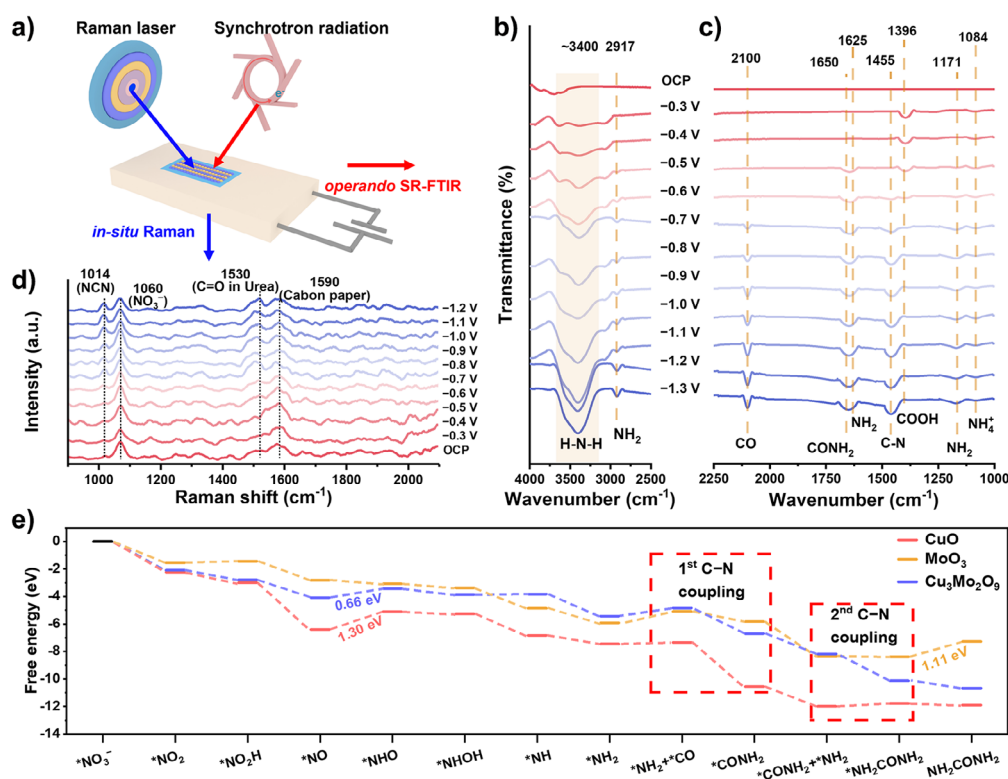


**Figure 3.** Mechanistic study. a) Schematic diagram of Operando SR-FTIR and in situ Raman techniques. Operando SR-FTIR spectra of Cu<sub>3</sub>Mo<sub>2</sub>O<sub>9</sub> collected under various applied potentials in the range of b) 4000–2500 cm<sup>-1</sup> and c) 2250–1000 cm<sup>-1</sup>. d) In situ Raman spectra of Cu<sub>3</sub>Mo<sub>2</sub>O<sub>9</sub> during urea electrosynthesis test. e) Free-energy diagram for urea production on the Cu<sub>3</sub>Mo<sub>2</sub>O<sub>9</sub>, CuO, and MoO<sub>3</sub>.

DEMS measurements on Cu<sub>3</sub>Mo<sub>2</sub>O<sub>9</sub> for individual NO<sub>3</sub>RR and CO<sub>2</sub>RR processes, the higher NH<sub>2</sub><sup>+</sup> and CO<sup>+</sup> signals can be detected, respectively, in contrast with those obtained from the co-electrolysis of NO<sub>3</sub><sup>-</sup> and CO<sub>2</sub> (Figures S14–S17). In combination with the emergence of CONH<sub>2</sub><sup>+</sup> signal, the abovementioned difference confirms that \*CO and \*NH<sub>2</sub> are the determinant intermediates for C–N coupling. The isotope-labelled DEMS measurements by replacing <sup>14</sup>NO<sub>3</sub><sup>-</sup> with <sup>15</sup>NO<sub>3</sub><sup>-</sup> presents the CO<sup>15</sup>NH<sub>2</sub><sup>+</sup> signal (*m/z* = 45), which further verify the formation of C–N bond by coupling \*CO with \*NH<sub>2</sub> on Cu<sub>3</sub>Mo<sub>2</sub>O<sub>9</sub> catalyst (for details, please see corresponding discussion and Figures S18–S19 in Supporting Information). On the basis of the above results, it infers that the “active hydrogen pump” supplies sufficient \*H for NO<sub>3</sub>RR and CO<sub>2</sub>RR during the co-electrolysis of NO<sub>3</sub><sup>-</sup> and CO<sub>2</sub> on Cu<sub>3</sub>Mo<sub>2</sub>O<sub>9</sub>, which can promote the production of key intermediates for C–N coupling.

To further uncover the C–N coupling mechanism of Cu<sub>3</sub>Mo<sub>2</sub>O<sub>9</sub>, operando synchrotron-radiation Fourier transform infrared spectroscopy (SR-FTIR) and in situ Raman were employed to monitor the real-time reaction intermediates during the urea electrosynthesis (Figure 3a). Infrared signals in the range of 1000 to 4000 cm<sup>-1</sup> were recorded with the applied potential from -0.3 V to -1.3 V versus RHE (Figure S20). The H–N–H stretching mode and N–H stretching mode at ~3400 and 2917 cm<sup>-1</sup> gradually increase with the negative shift of the applied potential (Figure 3b), which signifies the formation of \*NH<sub>2</sub> intermediates.<sup>[55]</sup> For

the range from 2250 to 1000 cm<sup>-1</sup>, the infrared bands at 1625 and 1170 cm<sup>-1</sup> correspond to the bending mode and rocking mode of –NH<sub>2</sub> in urea (Figure 3c).<sup>[56,57]</sup> Additionally, the disappearance of the stretching vibrational modes for –COOH at 1396 cm<sup>-1</sup> and the subsequent appearance of CO at 2100 cm<sup>-1</sup> suggest the \*CO<sub>2</sub> → \*COOH → \*CO pathway to produce C-containing intermediate.<sup>[20,58]</sup> These findings showcase the activation and reduction of CO<sub>2</sub>/NO<sub>3</sub><sup>-</sup> in the electrochemical process.<sup>[59]</sup> Notably, the infrared bands at 1455 and 1650 cm<sup>-1</sup> are identified as the C–N bond and CO–NH<sub>2</sub> bond, respectively,<sup>[60,61]</sup> which verifies that C–N bond formation originates from the coupling of \*CO and \*NH<sub>2</sub> intermediates. Similarly, in situ Raman spectra show the gradually increased intensities of the versus (C–N) (1014 cm<sup>-1</sup>) and –NH<sub>2</sub> (1510 cm<sup>-1</sup>) bending vibration when shifting to more negative potentials (Figure 3d).<sup>[65]</sup> Accordingly, the comprehensive understanding based on online DEMS, operando SR-FTIR and in situ Raman elucidates that \*CO and \*NH<sub>2</sub> are the key intermediates for C–N coupling on Cu<sub>3</sub>Mo<sub>2</sub>O<sub>9</sub> during the co-electrolysis of NO<sub>3</sub><sup>-</sup> and CO<sub>2</sub> process.

DFT calculations were employed to further examine the lowest energy pathway for the urea production process on the Cu<sub>3</sub>Mo<sub>2</sub>O<sub>9</sub>, CuO and MoO<sub>3</sub> catalysts. Initially, NO<sub>3</sub><sup>-</sup> will be reduced to produce \*NH<sub>2</sub> following the completion of the deoxidation and hydrogenation process (Figure 3e). Subsequently, the \*NH<sub>2</sub> intermediate can couple with \*CO to form \*CONH<sub>2</sub> intermediate, which is consistent with the experimental findings. In the urea electrosynthesis pathways,

the protonation of  $^*\text{NO}$  ( $^*\text{NO} \rightarrow ^*\text{NOH}$ ) is identified as the RDS for  $\text{Cu}_3\text{Mo}_2\text{O}_9$  and  $\text{CuO}$  catalysts. In contrast with  $\text{CuO}$  (1.30 eV),  $\text{Cu}_3\text{Mo}_2\text{O}_9$  requires a lower energy increase (0.66 eV) for  $^*\text{NOH}$  generation. This demonstrates that  $\text{Cu}_3\text{Mo}_2\text{O}_9$  enhances the  $\text{NO}_3\text{RR}$  activity to produce  $^*\text{NH}_2$  intermediates and thus increase the possibility of the C–N coupling between  $^*\text{CO}$  and  $^*\text{NH}_2$ . Although  $\text{MoO}_3$  had a lower  $\Delta G$  for  $^*\text{NH}_2$  generation, the  $^*\text{H}$  itself favors the HER process (Figure 2a). As elucidated by above DFT calculations and in situ spectroscopic analysis, as-engineered “active hydrogen pump”  $\text{Cu}_3\text{Mo}_2\text{O}_9$  catalyst can provide sufficient  $^*\text{H}$  for the formation of vital  $^*\text{CO}$  and  $^*\text{NH}_2$  intermediates. This boosts the C–N bond generation by coupling  $^*\text{CO}$  with  $^*\text{NH}_2$ , which may lead to exceptional urea electrosynthesis performance.

### Urea Electrosynthesis Performance

The urea electrosynthesis performance was first evaluated in an H-cell with a standard three-electrode system. As recorded by LSV, a higher current density is observed for the catalysts in the  $\text{CO}_2$ -saturated 0.1 M  $\text{KNO}_3$  compared to those in either the Ar-saturated or  $\text{CO}_2$ -saturated 0.1 M  $\text{Na}_2\text{SO}_4$  electrolytes, suggesting the co-reduction of  $\text{CO}_2$  and  $\text{NO}_3^-$  within the system (Figure 4b and Figure S21).<sup>[59]</sup> Furthermore,  $\text{Cu}_3\text{Mo}_2\text{O}_9$  exhibits a higher current density than  $\text{CuO}$  and  $\text{MoO}_3$  within the applied potential range, suggesting its higher activity toward urea electrosynthesis.<sup>[61]</sup>

Subsequently, the urea electrosynthesis performance was assessed using chronoamperometry across a potential range of  $-0.6$  to  $-1.0$  V versus RHE in a 0.1 M  $\text{KNO}_3$  electrolyte with  $20 \text{ mL min}^{-1}$   $\text{CO}_2$  bubbling into the catholyte (The optimization experiments of the  $\text{KNO}_3$  concentration and  $\text{CO}_2$  flow rate were described in the Supporting Information, Figures S22 and S23). Gas chromatography was employed to analyze the gaseous products, while ultraviolet-visible (UV–vis) spectroscopy was utilized to quantify products dissolved in the liquid (Figures S24–S26). The  $\text{Cu}_3\text{Mo}_2\text{O}_9$  catalyst delivers a volcano-shaped dependence of urea yield under the applied potentials (Figure 4a), achieving a peak urea yield rate of  $78.68 \text{ mmol h}^{-1} \text{ g}_{\text{cat}}^{-1}$  at  $-0.8$  V versus RHE. It significantly exceeds the urea yield rates for  $\text{CuO}$  ( $14.41 \text{ mmol h}^{-1} \text{ g}_{\text{cat}}^{-1}$ ) and  $\text{MoO}_3$  ( $3.59 \text{ mmol h}^{-1} \text{ g}_{\text{cat}}^{-1}$ ) (Figures S27–S29). The urea yield rates calculated based on the  $^1\text{H}$  nuclear magnetic resonance (NMR) spectroscopy align with those obtained using the urease method (Figures S30 and S31). Additionally, qualitative confirmation of urea formation is achieved through  $^1\text{H}$  NMR analysis using  $\text{K}^{14}\text{NO}_3$  or  $\text{K}^{15}\text{NO}_3$  as the nitrogen source. Distinct peaks indicative of urea formation are observed, including a single broad peak at 5.65 ppm for  $\text{CO}^{(14)}\text{NH}_2)_2$  as well as the doublet peaks at 5.62 and 5.72 ppm for  $\text{CO}^{(15)}\text{NH}_2)_2$  (Figure S32), which verifies the origin of nitrogen in as-produced urea. Control experiments exclude the detection of urea in the absence of  $\text{CO}_2$ ,  $\text{NO}_3^-$ , catalyst, or applied potential (Figures S33–S35). The potential by-product  $\text{N}_2\text{H}_4$  is evaluated using the Watt and Chrisp method, and the UV–vis spectrum reveals no distinct  $\text{N}_2\text{H}_4$  peak (Figures S36 and S37). These validate that

the detected urea indeed stems from the urea electrosynthesis process by coupling  $\text{CO}_2$  and  $\text{NO}_3^-$  on  $\text{Cu}_3\text{Mo}_2\text{O}_9$ , rather than from external sources such as carbon paper, feed gas, or surface contamination.

Apart from urea, by-products including ammonia ( $\text{NH}_3$ ), nitrite ( $\text{NO}_2^-$ ),  $\text{H}_2$ , and trace amounts of  $\text{CO}$  are detected for  $\text{Cu}_3\text{Mo}_2\text{O}_9$ ,  $\text{CuO}$ , and  $\text{MoO}_3$  (Figures S38–S40). Thereinto,  $\text{Cu}_3\text{Mo}_2\text{O}_9$  achieved a maximum urea FE of 26% at  $-0.8$  V versus RHE (Figure 4c), which indicates its higher C–N coupling selectivity during the urea electrosynthesis process compared to  $\text{CuO}$  and  $\text{MoO}_3$  catalysts (Figure S41). This result is in accordance with the above DFT calculations. Electrochemically active surface area (ECSA) was normalized using electrochemical double-layer capacitance ( $C_{\text{dl}}$ ) measurements. Similar ECSA results for  $\text{Cu}_3\text{Mo}_2\text{O}_9$ ,  $\text{CuO}$ , and  $\text{MoO}_3$  suggest that the outstanding urea electrosynthesis performance of  $\text{Cu}_3\text{Mo}_2\text{O}_9$  should be originated from its inherent activity (Figure S42). Product distributions reveal that  $\text{CuO}$  primarily produces  $\text{NO}_2^-$  and  $\text{NH}_3$  by-products, while  $\text{MoO}_3$  catalyst predominantly proceeds the HER process (Figure 4c and Figures S38 and S39). Attributed to the promoted hydrogenation,  $\text{Cu}_3\text{Mo}_2\text{O}_9$  can produce more  $^*\text{NH}_2$  intermediates for selective C–N coupling as reflected in less  $\text{NO}_2^-$  and  $\text{NH}_3$ . Other than facilitating the urea production, the supply of sufficient  $^*\text{H}$  also improves the amounts of  $\text{H}_2$  and  $\text{CO}$  (Figure 4c and Figure S40). The  $^*\text{H}$  quenching test with the addition of tertiary butanol (TBA) shows the decrease in the yields of  $\text{NO}_2^-$ ,  $\text{NH}_3$ ,  $\text{CO}$ , and urea for  $\text{Cu}_3\text{Mo}_2\text{O}_9$  when increasing the TBA concentration (Figure S43). The Tafel slopes are approximately or exceed  $120 \text{ mV dec}^{-1}$  (Figure 2c), indicating that the first electron transfer in nitrate activation might be the RDS at low overpotentials.<sup>[46,62]</sup> According to the quasi-equilibrium Langmuir adsorption model, the RDS mainly involves the consumption of one proton. Based on the above results, the  $\text{NO}_3\text{RR}$  and  $\text{CO}_2\text{RR}$  pathways involve hydrogen-mediated reduction processes rather than electron transfer-mediated reduction,<sup>[46,63]</sup> which will accelerate the hydrogenation of N- and C-intermediates into  $^*\text{NH}_2$  and  $^*\text{CO}$ , respectively. Thereby, the likelihood of C–N coupling will be increased for realizing selective urea electrosynthesis.

To further highlight the role of  $^*\text{H}$  in enhancing urea synthesis performance for  $\text{Cu}_3\text{Mo}_2\text{O}_9$ , control experiments were conducted to assess their activity for  $\text{NO}_3\text{RR}$  and  $\text{CO}_2\text{RR}$  separately. In the individual  $\text{NO}_3\text{RR}$  tests, argon gas instead of  $\text{CO}_2$  was fed into the electrolyte. Over the  $\text{CuO}$  catalyst,  $\text{NO}_2^-$  is detected as the major product (Figure S44), while  $\text{H}_2$  formation predominates on  $\text{MoO}_3$  with a FE of nearing 100% at the applied potential range (Figure S45). Unlike  $\text{CuO}$  catalyst,  $\text{Cu}_3\text{Mo}_2\text{O}_9$  exhibits an increased  $\text{NH}_3$ -producing FE accompanied with less  $\text{NO}_2^-$  (Figure S46). Benefiting from the “active hydrogen pump”, the  $\text{NO}_2^-$  will be further hydrogenated by  $^*\text{H}$  to allow the supply of the key  $^*\text{NH}_2$  intermediate. When meeting  $^*\text{CO}$  derived from  $\text{CO}_2\text{RR}$  after introducing  $\text{CO}_2$  as a reactant, the  $^*\text{NH}_2$  will favor C–N coupling with the  $^*\text{CO}$  intermediate for selective urea electrosynthesis over  $\text{Cu}_3\text{Mo}_2\text{O}_9$ , which results in the decreased FEs and yields of both  $\text{NO}_2^-$  and  $\text{NH}_3$  (Figures S47 and S48). For individual  $\text{CO}_2\text{RR}$  experiments,

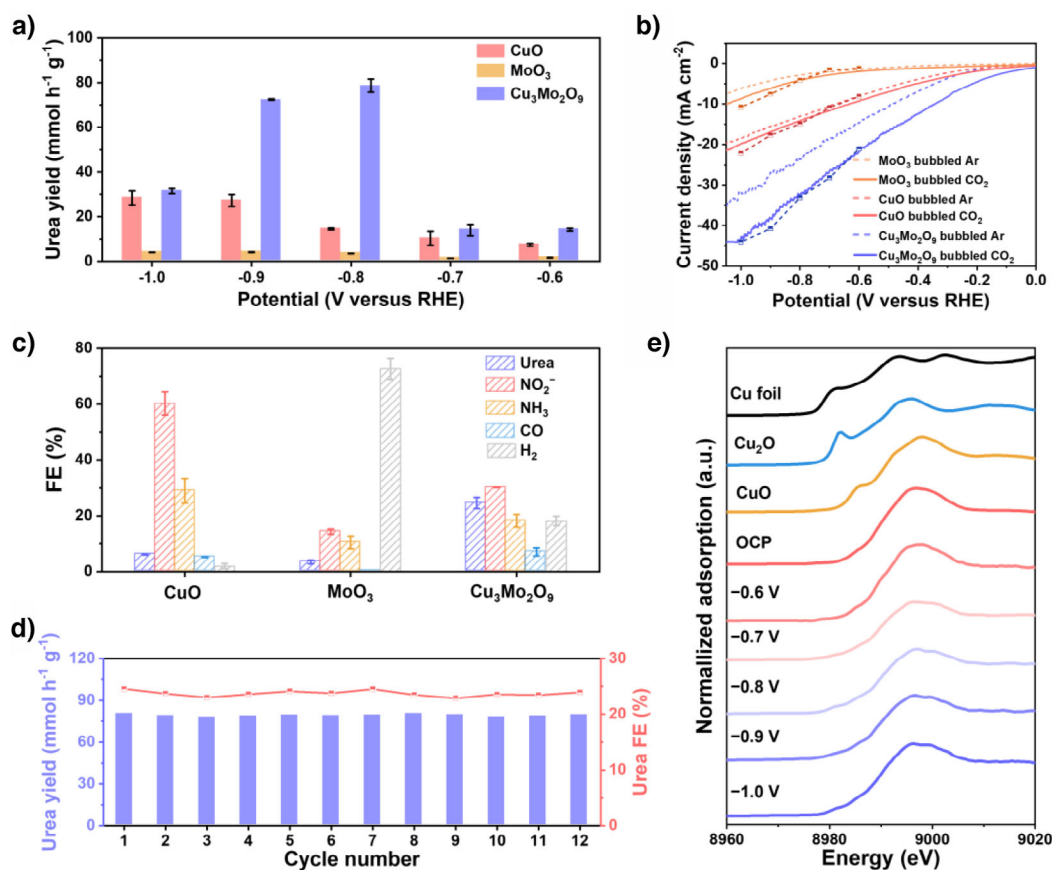


**Figure 4.** Urea electro-synthesis performance in H-cell. a) Urea yield rates at different potentials in 0.1 M  $\text{KNO}_3$  electrolyte with  $\text{CO}_2$  feeding gas. b) LSV curves in 0.1 M  $\text{KNO}_3$  with Ar or  $\text{CO}_2$  bubbling, and I–V plots in 0.1 M  $\text{KNO}_3$  with  $\text{CO}_2$  at different potentials. c) FEs of different products for CuO,  $\text{MoO}_3$  and  $\text{Cu}_3\text{Mo}_2\text{O}_9$  at  $-0.8$  V versus RHE in 0.1 M  $\text{KNO}_3$  electrolyte with  $\text{CO}_2$  feeding gas. d)  $\text{NH}_3$  yields and corresponding FEs for  $\text{Cu}_3\text{Mo}_2\text{O}_9$  during the long-term durability test. e) Cu K-edge in situ XANES spectra during the electrochemical urea electro-synthesis of  $\text{Cu}_3\text{Mo}_2\text{O}_9$  catalyst.

$\text{Cu}_3\text{Mo}_2\text{O}_9$  delivers higher CO yield and FE in contrast with CuO and  $\text{MoO}_3$  (Figures S49–S52). Additionally, CO-temperature-programmed gas desorption (CO-TPD) results indicate the strong signal intensity as well as high desorption temperature for  $\text{Cu}_3\text{Mo}_2\text{O}_9$  (Figure S53). As displayed in Figure S54,  $\text{Cu}_3\text{Mo}_2\text{O}_9$  does not show stronger  $\text{CO}_2$  adsorption in contrast with CuO and  $\text{MoO}_3$ , excluding the influence of  $\text{CO}_2$  adsorption and activation on the catalysis performance. In combination with the  $\text{CO}_2\text{RR}$  experiments, the above results infer that  $\text{Cu}_3\text{Mo}_2\text{O}_9$  can also provide sufficient and stabilized  $^*\text{CO}$  intermediate for C–N coupling. To further highlight the significant role of “active hydrogen pump” for  $\text{Cu}_3\text{Mo}_2\text{O}_9$ , we also synthesized the CuO/ $\text{MoO}_3$  catalyst (for details, please see corresponding discussion and Figures S55–S57 in Supporting Information). However, the maximum urea production rate ( $35.2 \text{ mmol h}^{-1} \text{ g}_{\text{cat}}^{-1}$ ) and the corresponding urea-producing FE (11.0%) of the CuO/ $\text{MoO}_3$  catalyst are much lower than those of  $\text{Cu}_3\text{Mo}_2\text{O}_9$ . The product distribution shows that the  $\text{NO}_2^-$  and  $\text{H}_2$  are the main byproducts, indicating the produced  $^*\text{H}$  by CuO/ $\text{MoO}_3$  is not supplied for  $\text{NO}_3\text{RR}$  and  $\text{CO}_2\text{RR}$  to promote the generation of  $^*\text{NH}_2$  and  $^*\text{CO}$ . Therefore, the “active hydrogen pump” behavior is crucial for the urea electro-synthesis process over  $\text{Cu}_3\text{Mo}_2\text{O}_9$ .

To evaluate the durability and reproducibility of the  $\text{Cu}_3\text{Mo}_2\text{O}_9$  catalyst in urea electro-synthesis, we conducted 12 continuous testing cycles (Figure 4d). The urea yield rates remain consistently high at approximately  $80 \text{ mmol h}^{-1} \text{ g}^{-1}$  with an average FE of 26%, demonstrating excellent electrochemical stability. During urea electro-synthesis, the Cu local structure was continuously monitored using in situ X-ray absorption spectroscopy (XAS). According to XANES spectra of the Cu K-edge (Figure 4e), the near-edge absorption energies of  $\text{Cu}_3\text{Mo}_2\text{O}_9$  remain consistent at the applied potential of  $-0.6$  to  $-1.0$  V versus RHE during the electrolysis, indicating no significant change in the valence state. The stability of  $\text{Cu}_3\text{Mo}_2\text{O}_9$  can also be explained by “active hydrogen pump” behavior, which accelerates the hydrogenation processes and electron transfer to avoid self-reconstruction and  $\text{NO}_2^-$  accumulation.<sup>[6]</sup> Characterization techniques, including XRD, SEM, TEM HRTEM, SAED, HAADF-STEM, and XPS confirm the exceptional stability of the  $\text{Cu}_3\text{Mo}_2\text{O}_9$  catalyst in its crystalline phase and nanostructure (Figures S58–S61).

Generally, a flow cell with gas diffusion electrode (GDE) (Figure 5a) is considered effective for catalytic reactions at the gas-solid interface, as the current density in a typical H-cell is limited due to the low solubility and slow dynamics of



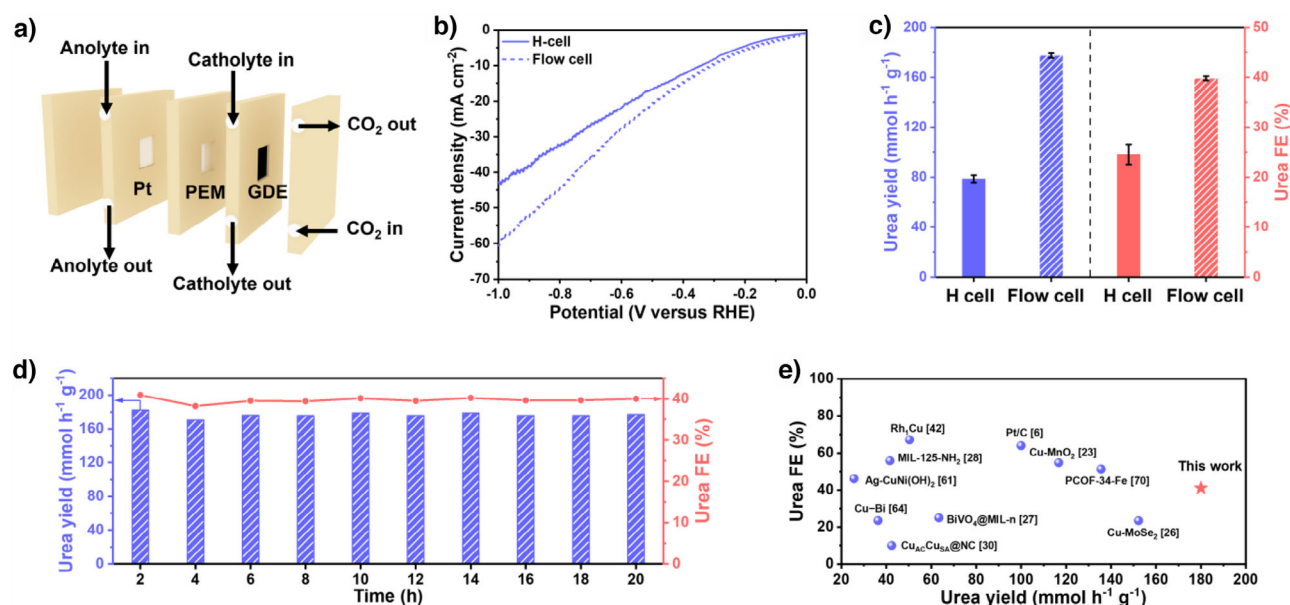


**Figure 5.** Urea electrosynthesis performance in flow cell. a) Schematic diagram of the flow cell. b) LSV curves of  $\text{Cu}_3\text{Mo}_2\text{O}_9$  in H-cell and flow cell. c) Urea yields and urea FEs of  $\text{Cu}_3\text{Mo}_2\text{O}_9$  in H-cell and flow cell at  $-0.8$  V versus RHE. d) The durability and reproducibility of the  $\text{Cu}_3\text{Mo}_2\text{O}_9$  catalyst toward urea electrosynthesis in flow cell. e) Electrochemical performance comparison between  $\text{Cu}_3\text{Mo}_2\text{O}_9$  and reported catalysts.

gas-phase reaction molecules.<sup>[64]</sup> Equipped by the flow cell,  $\text{Cu}_3\text{Mo}_2\text{O}_9$  delivers an enhanced current density compared to the H-cell (Figure 5b), suggesting the possible promoted urea electrosynthesis activity. Quantitative measurements reveal that  $\text{Cu}_3\text{Mo}_2\text{O}_9$  achieves a maximum urea yield of  $177 \text{ mmol h}^{-1} \text{ g}^{-1}$  with an excellent urea FE of 40% at  $-0.8$  V versus RHE in the flow cell (Figure 5c and Figure S62), which surpasses that in the H-cell. Furthermore, the yields and FEs of  $\text{NO}_2^-$  in the flow cell significantly decrease compared to those in the H-cell. The results might be attributed to the efficient mass transfer at the electrolyte/catalyst interface during the urea electrosynthesis process. The sufficient  $^*\text{H}$  provided by the “active hydrogen pump” catalyst will accelerate the hydrogenation of C- and N-containing species to generate  $^*\text{CO}$  and  $^*\text{NH}_2$  intermediates, thereby expediting the C–N bond formation. During a 20 h continuous test, no significant current decay in current-time ( $I$ - $t$ ) curve further highlights the endurance of  $\text{Cu}_3\text{Mo}_2\text{O}_9$  (Figure S64a). Remarkably, both the urea yield rates and FEs remain stable within 20 h (Figure 5d and Figure S64b), proving  $\text{Cu}_3\text{Mo}_2\text{O}_9$  as an exceptional and stable catalyst for urea electrosynthesis. In sharp contrast, the urea electrosynthesis performance of as-designed “active hydrogen pump” catalyst outperforms most recently reported catalysts in the literatures (Figure 5e).<sup>[6,25,29,56,59,65]</sup>

## Conclusion

To summarize, we developed a  $\text{Cu}_3\text{Mo}_2\text{O}_9$  nanorod catalyst for urea synthesis through the co-electrolysis of  $\text{NO}_3^-$  and  $\text{CO}_2$  under ambient conditions. By regulating the water dissociation and hydrogen adsorption, as-developed  $\text{Cu}_3\text{Mo}_2\text{O}_9$  played a role as “active hydrogen pump” catalyst to supply sufficient  $^*\text{H}$  for promoting the hydrogenation of  $\text{NO}_3^-$  and

$\text{CO}_2$ , which was validated by DFT calculations in combination with quasi-in situ EPR experiments. As recorded by a series of in situ analysis, including operando SR-FTIR, isotope-labelled DEMS, and in situ Raman analysis,  $^*\text{CO}$  and  $^*\text{NH}_2$  were the vital intermediates derived from hydrogenation processes for selective C–N coupling. In a  $\text{CO}_2$ -saturated 0.1 M  $\text{KNO}_3$  solution,  $\text{Cu}_3\text{Mo}_2\text{O}_9$  delivered a maximum urea yield of  $177 \text{ mmol h}^{-1} \text{ g}^{-1}$  with a high urea FE of 40% at  $-0.8$  V versus RHE in the flow cell, which surpassed most reported literatures. This work not only emphasizes the crucial role of  $^*\text{H}$  for intermediates hydrogenation, but also provide a viable way to engineer achievable Cu-based catalysts for efficient urea electrosynthesis from  $\text{CO}_2$  and  $\text{NO}_3^-$ .

## Acknowledgements

C.L. acknowledges the National Natural Science Foundation of China (52302231 and 22479034), and Key Research & Development Plan of Heilongjiang Province (2024ZXJ03C06). C.Y. acknowledges the National Natural Science Foundation of China (52101246), and the Natural Science Foundation of Heilongjiang Province, China (YQ2022B006). Q. Yan acknowledges funding support from Singapore MOE AcRF Tier 1 grant RT6/22 and RG8/24, Low Carbon Energy Research (LCER) Phase 2: Directed Hydrogen Programme: award number U2305D4001. L.S. acknowledges the National Natural Science Foundation of China (124B2110). The authors thank the BL14W1 beamline of Shanghai Synchrotron Radiation Facility (SSRF). The authors thank the Hefei Synchrotron Radiation Facility (BL01B Infrared spectroscopy and microspectroscopy, BL12B, MCD-A and MCD-B). The authors thank the Anhui Absorption Spectroscopy Analysis Instrument Co, Ltd. for in situ XAFS measurements and analysis. The authors thank the



Hefei advanced computing center. Thanks sci-go ([www.sci-go.com](http://www.sci-go.com)) for the XPS and TEM characterizations, and TPD measurement.

### Conflict of Interests

The authors declare no conflict of interest.

### Data Availability Statement

The data that support the findings of this study are available from the corresponding author upon reasonable request.

**Keywords:** Active hydrogen • C–N coupling • Copper-based electrocatalysts • Intermediates hydrogenation • Urea electrosynthesis

- [1] P. Garrido-Barros, J. Derosa, M. J. Chalkley, J. C. Peters, *Nature* **2022**, 609, 71–76.
- [2] X. Zhang, E. A. Davidson, D. L. Mauzerall, T. D. Searchinger, P. Dumas, Y. Shen, *Nature* **2015**, 528, 51–59.
- [3] J. Liu, Z. Li, C. Lv, X.-Y. Tan, C. Lee, X. J. Loh, M. H. Chua, Z. Li, H. Pan, J. Chen, Q. Zhu, J. Xu, Q. Yan, *Mater. Today* **2024**, 73, 208–259.
- [4] C. Lv, J. Liu, C. Lee, Q. Zhu, J. Xu, H. Pan, C. Xue, Q. Yan, *ACS Nano* **2022**, 16, 15512–15527.
- [5] Y. Zhao, Y. Ding, W. Li, C. Liu, Y. Li, Z. Zhao, Y. Shan, F. Li, L. Sun, F. Li, *Nat. Commun.* **2023**, 14, 4491.
- [6] H. Xiong, P. Yu, K. Chen, S. Lu, Q. Hu, T. Cheng, B. Xu, Q. Lu, *Nat. Catal.* **2024**, 7, 785–795.
- [7] C. Zhang, Q. Wang, Z. Li, H. Liu, L. Zhong, J. Liu, Z. Wang, R. Wu, P. Song, W. J. Chen, Z. Qi, C. Yan, L. Song, Q. Yan, C. Lv, *Angew. Chem. Int. Ed.* **2025**, 64, e202502957.
- [8] Z. Li, Q. Wang, L. Zhong, C. Yan, Z. Shi, Y. Ou, Y. Shang, C. Zhang, S. Tian, H. Liu, D. Liu, P. Song, Z. Qi, L. Song, C. Lv, *Mater. Today* **2025**, 85, 49–59.
- [9] C. Lv, C. Yan, G. Chen, Y. Ding, J. Sun, Y. Zhou, G. Yu, *Angew. Chem. Int. Ed.* **2018**, 57, 6073–6076.
- [10] C. Lv, L. Zhong, H. Liu, Z. Fang, C. Yan, M. Chen, Y. Kong, C. Lee, D. Liu, S. Li, J. Liu, L. Song, G. Chen, Q. Yan, G. Yu, *Nat. Sustain.* **2021**, 4, 868–876.
- [11] X. Wei, Y. Liu, X. Zhu, S. Bo, L. Xiao, C. Chen, T. T. T. Nga, Y. He, M. Qiu, C. Xie, D. Wang, Q. Liu, F. Dong, C. L. Dong, X. Z. Fu, S. Wang, *Adv. Mater.* **2023**, 35, 2300020.
- [12] C. Lv, Y. Qian, C. Yan, Y. Ding, Y. Liu, G. Chen, G. Yu, *Angew. Chem. Int. Ed.* **2018**, 57, 10246–10250.
- [13] C. Chen, X. Zhu, X. Wen, Y. Zhou, L. Zhou, H. Li, L. Tao, Q. Li, S. Du, T. Liu, D. Yan, C. Xie, Y. Zou, Y. Wang, R. Chen, J. Huo, Y. Li, J. Cheng, H. Su, X. Zhao, W. Cheng, Q. Liu, H. Lin, J. Luo, J. Chen, M. Dong, K. Cheng, C. Li, S. Wang, *Nat. Chem.* **2020**, 12, 717–724.
- [14] Y. Wang, S. Xia, K. Chen, J. Zhang, C. Yu, J. Wu, P. Wang, W. Zhang, Y. Wu, *Angew. Chem. Int. Ed.* **2025**, 64, e202503011.
- [15] L. Zheng, Y. Zhang, W. Chen, X. Xu, R. Zhang, X. Ren, X. Liu, W. Wang, J. Qi, G. Wang, C. Ma, L. Xu, P. Han, Q. He, D. Ma, J. Wang, C. Ling, D. Su, M. Shao, Y. Chen, *Angew. Chem. Int. Ed.* **2025**, 64, e202500985.
- [16] X. Ouyang, W. Qiao, Y. Yang, B. Xi, Y. Yu, Y. Wu, J. Fang, P. Li, S. Xiong, *Angew. Chem. Int. Ed.* **2025**, 64, e202422585.
- [17] X. Liu, Y. Jiao, Y. Zheng, M. Jaroniec, S.-Z. Qiao, *Nat. Commun.* **2022**, 13, 5471.
- [18] H. Yin, Z. Sun, Q. Zhao, L. Yang, T. Lu, Z. Zhang, *J. Energy Chem.* **2023**, 84, 385–393.
- [19] C. Lv, C. Lee, L. Zhong, H. Liu, J. Liu, L. Yang, C. Yan, W. Yu, H. H. Hng, Z. Qi, L. Song, S. Li, K. P. Loh, Q. Yan, G. Yu, *ACS Nano* **2022**, 16, 8213–8222.
- [20] D.-S. Huang, X.-F. Qiu, J.-R. Huang, M. Mao, L. Liu, Y. Han, Z.-H. Zhao, P.-Q. Liao, X.-M. Chen, *Nat. Synth.* **2024**, 3, 1404–1413.
- [21] X. Zhang, H. Sun, Y. R. Wang, Z. Shi, R. L. Zhong, C. Y. Sun, J. Y. Liu, Z. M. Su, Y. Q. Lan, *Adv. Mater.* **2024**, 36, 202408510.
- [22] Y. Yang, G. Wu, J. Jiang, W. Zhang, S. Liu, R. Yu, F. Liu, A. Du, L. Dai, X. Mao, Q. Qin, *Adv. Mater.* **2024**, 36, 2409697.
- [23] Z. Dai, Y. Chen, H. Zhang, M. Cheng, B. Zhang, P. Feng, Y. Feng, G. Zhang, *Nat. Commun.* **2025**, 16, 3271.
- [24] Y. Tan, J. Fu, T. Luo, K. Liu, M. Liu, *J. Am. Chem. Soc.* **2025**, 147, 4937–4944.
- [25] J. Jiang, G. Wu, M. Sun, Y. Liu, Y. Yang, A. Du, L. Dai, X. Mao, Q. Qin, *ACS Nano* **2024**, 18, 13745–13754.
- [26] S. Yao, S. Y. Jiang, B. F. Wang, H. Q. Yin, X. Y. Xiang, Z. Tang, C. H. An, T. B. Lu, Z. M. Zhang, *Angew. Chem. Int. Ed.* **2025**, 64, e202418637.
- [27] X. Huang, Y. Li, S. Xie, Q. Zhao, B. Zhang, Z. Zhang, H. Sheng, J. Zhao, *Angew. Chem. Int. Ed.* **2024**, 63, e202403980.
- [28] Y. Li, Y. Sun, M. Yu, *Adv. Funct. Mater.* **2024**, 34, 2410186.
- [29] X. Ma, B. Mao, Z. Yu, D. Wang, J. Xia, J. Hou, X. Meng, H. Lin, C. Hu, *Angew. Chem. Int. Ed.* **2025**, 64, e202423706.
- [30] C. Zhao, Y. Jin, J. Yuan, Q. Hou, H. Li, X. Yan, H. Ou, G. Yang, *J. Am. Chem. Soc.* **2025**, 147, 8871–8880.
- [31] Z. Li, Y. Wang, H. Liu, Y. Feng, X. Du, Z. Xie, J. Zhou, Y. Liu, Y. Song, F. Wang, M. Sui, Y. Lu, F. Fang, D. Sun, *Nat. Mater.* **2025**, 24, 424–432.
- [32] I. E. Stewart, S. Ye, Z. Chen, P. F. Flowers, B. J. Wiley, *Chem. Mater.* **2015**, 27, 7788–7794.
- [33] L. Yu, H. Zhou, J. Sun, F. Qin, F. Yu, J. Bao, Y. Yu, S. Chen, Z. Ren, *Energy Environ. Sci.* **2017**, 10, 1820.
- [34] X. Su, F. Hong, Y. Fang, Y. Wen, B. Shan, *Angew. Chem. Int. Ed.* **2025**, 64, e202422072.
- [35] P. Liu, Y. Liang, X. Lin, C. Wang, G. Yang, *ACS Nano* **2011**, 5, 4748–4755.
- [36] Z. Xia, X. Tian, P. Xu, B. Cheng, H. Xu, S. Guang, *Chem. Eng. J.* **2024**, 496, 154078.
- [37] R. Cai, H. Zhu, F. Yang, M. Ju, X. Huang, J. Wang, M. D. Gu, J. Gao, S. Yang, *Angew. Chem. Int. Ed.* **2025**, 64, e202424098.
- [38] K. Liu, H. Shen, Z. Sun, Q. Zhou, G. Liu, Z. Sun, W. Chen, X. Gao, P. Chen, *Nat. Commun.* **2025**, 16, 1203.
- [39] S. Luo, J. Gao, C. Yin, Y. Lu, Y. Wang, *Nat. Commun.* **2025**, 16, 1114.
- [40] J. Xiang, C. Qiang, S. Shang, Y. Guo, K. Chu, *ACS Nano* **2024**, 18, 29856–29863.
- [41] A. Bhattacharjee, M. Ahmaruzzaman, *RSC Adv.* **2016**, 6, 41348.
- [42] Z. Li, L. Gao, S. Zheng, *Mater. Lett.* **2003**, 57, 4605–4610.
- [43] M. Sun, W. Wan, X. Zhao, C. Shao, N. Liu, M. Fan, J. Wang, *Adv. Funct. Mater.* **2025**, 2500553.
- [44] X. Wei, S.-Q. Liu, H. Liu, Y. Ding, P.-X. Lei, S. Wu, L. Song, X.-Z. Fu, J.-L. Luo, *J. Am. Chem. Soc.* **2025**, 147, 6049–6057.
- [45] P. Wang, D. Zhao, P. Zhang, X. Hui, Z. Zhang, R. Wang, C. Wang, X. Ge, X. Liu, Y. C. Li, L. Yin, *Nat. Commun.* **2025**, 16, 1453.
- [46] L. Bai, F. Franco, J. Timoshenko, C. Rettenmaier, F. Scholten, H. S. Jeon, A. Yoon, M. Rüschler, A. Herzog, F. T. Haase, S. Köhl, S. W. Chee, A. Bergmann, R. C. Beatriz, *J. Am. Chem. Soc.* **2024**, 146, 9665–9678.
- [47] S.-N. Zhang, P. Gao, Q.-Y. Liu, Z. Zhang, B.-L. Leng, J.-S. Chen, X.-H. Li, *Nat. Commun.* **2024**, 15, 10877.
- [48] Y. Wan, M. Pei, Y. Tang, Y. Liu, W. Yan, J. Zhang, R. Lv, *Adv. Mater.* **2025**, 37, 202417696.
- [49] X. Zhang, S. Xu, X. Li, T. Song, D. Ji, Q. Chen, *J. Am. Chem. Soc.* **2025**, 147, 11533–11542.

- [50] K. Chandra Majhi, H. Chen, A. Batool, Q. Zhu, Y. Jin, S. Liu, P. H. L. Sit, J. Chun-Ho Lam, *Angew. Chem. Int. Ed.* **2025**, *64*, e202500167.
- [51] J. Li, H. Li, K. Fan, J. Y. Lee, W. Xie, M. Shao, *Chem Catal* **2023**, *3*, 100638.
- [52] K. Fan, W. Xie, J. Li, Y. Sun, P. Xu, Y. Tang, Z. Li, M. Shao, *Nat. Commun.* **2022**, *13*, 7958.
- [53] Y. Guo, R. Zhang, S. Zhang, Y. Zhao, Q. Yang, Z. Huang, B. Dong, C. Zhi, *Energy Environ. Sci.* **2021**, *14*, 3938–3944.
- [54] F. Lyu, C. Liu, S. Zeng, X. Bu, Y. Chen, Z. Jia, Y. Xie, L. Sun, Z. Mao, J. Shen, G. Li, J. Luan, Y. Yan, L. Yao, L. Li, X. Wang, G. Wu, Y. Y. Li, J. Lu, *Energy Environ. Sci.* **2024**, *17*, 7908–7918.
- [55] D. Zhang, Y. Xue, X. Zheng, C. Zhang, Y. Li, *Natl. Sci. Rev.* **2023**, *10*, nwac209.
- [56] W. Ye, Y. Zhang, L. Chen, F. Wu, Y. Yao, W. Wang, G. Zhu, G. Jia, Z. Bai, S. Dou, P. Gao, N. Wang, G. Wang, *Angew. Chem. Int. Ed.* **2024**, *63*, e202410105.
- [57] M. Zhou, Y. Zhang, H. Li, Z. Li, S. Wang, X. Lu, S. Yang, *Angew. Chem. Int. Ed.* **2024**, *64*, e202414392.
- [58] Q. Hu, W. Zhou, S. Qi, Q. Huo, X. Li, M. Lv, X. Chen, C. Feng, J. Yu, X. Chai, H. Yang, C. He, *Nat. Sustain.* **2024**, *7*, 442–451.
- [59] X. Song, X. Ma, T. Chen, L. Xu, J. Feng, L. Wu, S. Jia, L. Zhang, X. Tan, R. Wang, C. Chen, J. Ma, Q. Zhu, X. Kang, X. Sun, B. Han, *J. Am. Chem. Soc.* **2024**, *146*, 25813–25823.
- [60] Y. Feng, H. Yang, Y. Zhang, X. Huang, L. Li, T. Cheng, Q. Shao, *Nano Lett.* **2020**, *20*, 8282–8289.
- [61] Y. Gao, J. Wang, M. Sun, Y. Jing, L. Chen, Z. Liang, Y. Yang, C. Zhang, J. Yao, X. Wang, *Angew. Chem. Int. Ed.* **2024**, *63*, e202402215.
- [62] B. Kang, B. Xu, Z. Chen, F. Li, Y. Wang, *Appl. Catal. B-Environ. Energy* **2025**, *360*, 124528.
- [63] R. Wang, S. Jia, L. Wu, L. Zhang, X. Song, X. Tan, C. Zheng, W. Li, X. Ma, Q. Qian, X. Kang, Q. Zhu, X. Sun, B. Han, *Angew. Chem. Int. Ed.* **2025**, *64*, e202425262.
- [64] C. Zhang, S. Chen, L. Guo, Z. Li, C. Yan, C. Lv, *Chinese J. Chem.* **2024**, *42*, 3441–3468.
- [65] C. Gong, Y. Peng, M. Xu, X. Wei, G. Sheng, J. Liu, X. Wu, X. Han, F. Dai, J. Dong, Z. Chen, Y. Zhu, W. Ye, Y. Cui, *Nat. Synth.* **2025**, <https://doi.org/10.1038/s44160-025-00742-6>.

Manuscript received: April 08, 2025

Revised manuscript received: May 04, 2025

Accepted manuscript online: May 12, 2025

Version of record online: ■■■■■

## Research Article

## Urea Electrosynthesis

C. Zhang, Q. Zhou, Z. Li, C. Yan\*,  
H. Liu, D. Liu\*, L. Song, Q. Yan\*,  
C. Lv\* ————— e202507869

Promoting the Intermediates  
Hydrogenation for Urea Electrosynthesis  
Over an “Active Hydrogen Pump” Catalyst

The  $\text{Cu}_3\text{Mo}_2\text{O}_9$  nanorods was developed to serve as “active hydrogen pump” electrocatalyst, which could regulate the water dissociation and hydrogen adsorption. Such electrocatalyst would guarantee a steady  $^*\text{H}$  supply for intermediates hydrogenation, hence boosting the generation of  $^*\text{CO}$  and  $^*\text{NH}_2$  intermediates for selective C—N coupling and urea production.

